Article

Model-Free Control for Doubly Salient Permanent Magnet-Generator-Based Tidal Stream Turbine Considering Flux-Weakening Operation

Hao Chen [1,*], Luming Liu [1], Yassine Amirat [2,*], Zhibin Zhou [2], Nadia Aït-Ahmed [3] and Mohamed Benbouzid [1,4]

1   The Research Institute of Power Drive and Control, Shanghai Maritime University, Shanghai 201306, China; 202130210105@stu.shmtu.edu.cn (L.L.); mohamed.benbouzid@univ-brest.fr (M.B.)
2   L@bISEN, ISEN Yncréa Ouest, 29200 Brest, France; zhibin.zhou@isen-ouest.yncrea.fr
3   Institut de Recherche en Energie Electrique de Nantes Atlantique, University of Nantes, 44602 Saint-Nazaire, France; nadia.ait-ahmed@univ-nantes.fr
4   Institut de Recherche Dupuy de Lôme (UMR CNRS 6027 IRDL), University of Brest, 29240 Brest, France
*   Correspondence: chenhao@shmtu.edu.cn (H.C.); yassine.amirat@isen-ouest.yncrea.fr (Y.A.)

Abstract: Renewable energy generation is increasingly important due to serious energy issues. A Doubly Salient Permanent Magnet Generator (DSPMG) can be an interesting candidate for tidal stream renewable energy systems. However, the special structure makes the system nonlinear and strongly coupled even after Park transformation and involves a larger torque ripple. Previous research mainly focused on model-based control for this machine, which is very sensitive to the parameters. Thus, to control the complex systems stably and accurately, two model-free control algorithms, Active Disturbance Rejection-Based Iterative Learning Control (ADRILC) and Active Disturbance Rejection Control–Iterative Learning Control (ADRC–ILC), are proposed for the current and speed control loops of a DSPMG-based Tidal Stream Turbine (TST), respectively. ADRC–ILC uses ADRC to deal with the external non-periodic speed ripple and adopts ILC to reduce the internal periodic speed ripple. ADRILC employs an iterative method to improve the ESO for the enhancement of the convergence rate of ILC. Considering the variable tidal speed, when the speed is above the rated value, Maximum Power Point Tracking (MPPT) must be changed to a power limitation strategy for limiting the generator power to the rated value and extending the system operating range. Thus, Optimal Tip Speed Ratio (OTSR)-based MPPT (for a low tidal current speed) and Leading Angle Flux-Weakening Control (LAFWC) (for a high tidal current speed) strategies are also proposed. According to the simulation results, the proposed ADRC–ILC + ADRILC has the lowest torque ripple, the highest control accuracy, as well as a good current tracking capability and strong robustness. At the rated speed, the proposed method reduces the torque ripple by more than 20% and the speed error by about 80% compared with PI control: the current difference is limited in 2A. The LAFWC proposed for an excessive tidal current speed is effective in conserving the electromagnetic power and increasing the generator speed.

Keywords: tidal stream turbine; doubly salient permanent magnet generator; model-free control; active disturbance rejection-based iterative learning control; maximum power point tracking; leading angle flux-weakening control

1. Introduction

With the global depletion of fossil energy and the serious problem of environmental pollution, the development of renewable energy is becoming particularly significant. Tidal current energy, which has high predictability and a high energy density, has made great progress in recent years. As gearboxes may increase the failure rate and make maintenance

difficult and expensive in complicated underwater working conditions, a direct-drive Tidal Stream Turbine (TST), which is coupled to a low-speed machine, is preferred [1,2].

A Doubly Salient Permanent Magnet Machine (DSPMM), first proposed in the 1990s, has the advantages of a simple structure, high unit volume density, high torque-to-current ratio, high efficiency and low manufacturing cost [3]. It can be widely adopted in electric vehicles and some other high-speed fields [4]. With the development of teeth coupling and magnetic gears, the DSPMM could also be used in low-speed and high-power applications, such as ship propulsion, wind turbines and TSTs [5–7].

According to the different forms of back Electromotive Force (EMF), the DSPMM operates in two modes: the Brushless DC (BLDC) and Brushless AC (BLAC) modes [4]. When it operates in BLDC mode, due to the special double salient structure, the fringing magnetic field effect and the sudden change in air gap magnetic field energy exist in the overlapping area of the salient pole surfaces. When the rotor passes the commutation point, it will cause a sudden drop in each phase torque and bring about a very serious torque ripple, which is also the cause of noise and vibration [8]. Because of the same variation period of PM flux linkage and inductance, when it operates in BLAC mode, the DSPMM would still have strong nonlinearity and coupling even after Park transformation. Moreover, a sinusoidal current is not sufficient to maintain a constant torque and causes periodic ripple.

Torque ripple leads to speed instabilities and increases the system's energy consumption. In addition, the huge torque ripple will also increase the wear of the mechanical parts. Undoubtedly, both modes could decrease the torque ripple and improve the system stability to a certain extent. In BLDC mode, due to the different and complex working conditions, the optimal conduction angles are difficult to determine. Certain control parameters should be optimized depending on the values found in simulations or experiments. In BLAC mode, the nonlinearity would make the system control complicated, and the compensated harmonic current is difficult to calculate if a constant torque is desired. According to the literature, as BLAC mode could eliminate the torque ripple theoretically, this should be a very attractive feature for low-speed and high-torque fields. Consequently, in this paper, the toothed-pole Doubly Salient Permanent Magnet Generator (DSPMG) in the TST will operate in BLAC mode.

BLAC mode prefers a machine with sinusoidal back EMF. Rotor-skewing and teeth-coupling technologies are usually used to make the waveforms of back EMF more sinusoidal [9,10]. W. Hua et al. adopted a vector-control strategy for this machine to establish a dq model of a DSPMM for the first time [11]. X. Pan et al. proposed a current loop control method based on a PI controller parallel resonant regulator to suppress the harmonics of the phase current and improve the stability of the machine [12]. However, the average torque slightly decreased. F. Liu et al. presented a resonance compensation control strategy to suppress the speed ripple of the DSPMM effectively [13]. Nevertheless, the torque ripple analysis is missing. W. Xu et al. proposed a model of predictive-control-based current and torque control [14,15]. Although these methods can achieve better stability, a faster dynamic response and smaller torque and flux ripple, they require high model accuracy. Y. Yang proposed a multiple sine-wave superposition (MSWS) driving method, and this method greatly improves the torque characteristics and the dynamic performance of a doubly salient motor compared with square-wave driving [16]. H Cheng et al. injected harmonic currents into the armature winding to compensate for the cogging torque to reduce the torque ripple [17]. H. Chen et al. deduced a quasi-sinusoidal current for a constant torque according to a performance comparison of the DSPMM under BLDC and BLAC modes, and designed First-Order Sliding Mode Control (FOSMC) and High-Order Sliding Mode Control (HOSMC) to deal with the nonlinear tracking and control of the current loop. The system had a good dynamic response and strong robustness [9,18,19]. Unfortunately, the calculation of the quasi-sinusoidal current is complex, and highly dependent on the machine parameters and the rotor position. The system robustness may also decrease due to the variation in the inductance.

In general, the majority of previous research has mainly focused on a model-based controller, which is very sensitive to the parameters. However, the parameters of the DSPMG will vary due to the flux saturation and the perturbations. Moreover, a mismatched model will also cause some torque ripple and may even deteriorate the system performance. Consequently, Model-Free Control (MFC), which is independent of the mathematical model, should be a highly anticipated potential solution for such a system.

The periodic torque ripples, caused by the current supply and parameter variations, are reflected as periodic oscillations in the machine speed, especially for low-speed operation. The non-periodic torque ripples due to the external environmental disturbances result in non-periodic speed ripples. All these torque ripples may make the rotor shaft suffer a high torsion, limit the system performance and even damage the system. Thus, it is important to minimize the periodic and non-periodic torque ripple and resulting speed ripple. For the speed–current closed-loop control, an ASR (Automatic Speed Regulator) is always used to generate the suitable current reference for the desired torque; the ACR (Automatic Current Regulator) mainly follows the current reference.

To reduce the periodic speed ripple of the DSPMG, Iterative Learning Control (ILC) could be very attractive. It can improve the transient and steady-state performance by operating repetitively over a fixed time interval and effectively reject the periodic disturbances consequently [20–22]. This means that this control could generate a proper current reference to minimize the periodic torque ripple theoretically. Considering the complex working conditions, the non-periodic speed ripple is inevitable in the system and will highly affect the ILC repetitive control and iterative effect, resulting in slower tracking or even tracking failures. Because Active Disturbance Rejection Control (ADRC) is robust to uncertain disturbances and can estimate and compensate for aperiodic disturbances online using an Extended State Observer (ESO), it should be a good supplementary for the non-periodic ripple [23,24].

Consequently, fusion control based on these two MFC methods, ADRC–ILC, is proposed for ASR. It uses ILC to compensate for the periodic disturbance, and adopts ADRC to deal with the non-periodic disturbance. It presents ADRC operating in parallel with the ILC. The sum of them is utilized to derive the desired current reference corresponding to the minimum speed ripple. Due to the complexity of the machine model, MFC for the ACR is also very essential. In this paper, Active Disturbance Rejection-Based Iterative Learning Control (ADRILC) is proposed to track the current reference quickly and accurately [25,26]. It adopts a Tracking Differentiator (TD) to achieve smooth current signals, and uses the iterative learning method to design the Iterative Extended State Observer (IESO) to estimate system uncertainties explicitly during the process of iterations and enhance the convergence rate of ILC.

Theoretically, this proposed control algorithm is suitable for a DSPMG with variable speed and torque. However, when the speed is higher than the rated value, the operation of the system must meet the constrains of current and voltage. Consequently, a flux-weakening control strategy should be adopted to adjust the current and extend the speed operating range for a DSPMG-based TST.

For the traditional PMSM, there are many studies on flux-weakening control to acquire the demagnetization current, such as the formulas method, the gradient descent method, the single current regulator method and the current lead angle method [27–31]. Before now, the research on the flux-weakening control strategy for DSPMMs has been very limited. Only some researchers have proposed certain special mechanical structures to change the flux [32,33]. As a DSPMM has no additional excitation coil, it weakens the magnetic field by adjusting the demagnetization component of the armature current. The flux-weakening control mechanism of a DSPMM is very similar to a PMSM, but also has some difficulties. In this paper, Leading Angle Flux-Weakening Control (LAFWC) with an anti-windup method is proposed for the DSPMG to ensure the stability of the system at an excessive speed.

Based on the discussion above, in this paper, Section 2 will introduce the mathematical models of a toothed-pole DSPMG-based TST. In Section 3, the ADRILC and ADRC–ILC

algorithms are discussed, proved and applied to the system. In Section 4, Optimal Tip Speed Ratio (OTSR)-based Maximum Power Point Tracking (MPPT) (for a low tidal current speed) and LAFWC strategies (for a high tidal current speed) are proposed for the system. Then, the control performance and robustness analyses of different control algorithms are presented and discussed in Section 5. In the last part, the concluding remarks of this work are presented.

2. TST Modeling

The basic principle of a TST is similar to that of wind turbine. Principally, the turbine is driven by the flowing tidal current to rotate, and then the power converter drives the generator as a controlled brake to generate electricity optimally. It should be noted that, compared to wind power generation, the tidal current has a greater energy density, higher efficiency and stronger regularity [19]. The whole general scheme of the TST is shown in Figure 1. The model of a DSPMG-based TST will be established in this section.
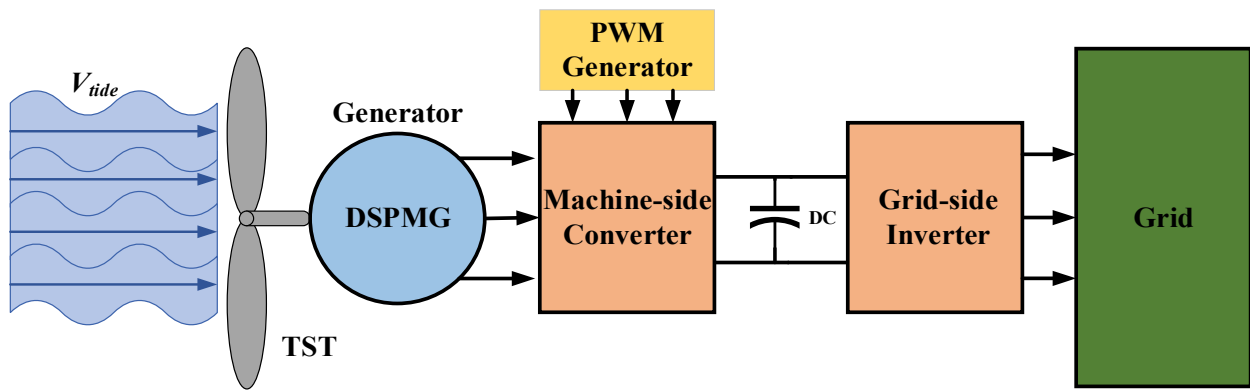

Figure 1. Global scheme of TST.

2.1. Turbine Modeling

The extractable mechanical power P_{TST} of the TST, which is converted from the hydrodynamic power P_{hyd}, is shown in Equation (1) [34,35].

$$P_{TST} = C_p P_{hyd} = \frac{1}{2} C_p \rho A V_{tide}^3 \tag{1}$$

where ρ is the fluid density; A is the swept area of the turbine; V_{tide} is the tidal current speed and C_p is the power coefficient, which determines the efficiency of the conversion of tidal current energy for this direct-drive TST.

2.2. DSPMG Modeling

In this paper, a DSPMG is used as the low-speed generator for the TST. This machine has four non-rotating PMs located at the stator. There are 48 small teeth distributed on 12 big teeth in the stator, and the rotor only includes 64 small teeth, which are regularly distributed. It is designed and optimized to achieve the maximum volume torque, is 45.5 kNm/m^3 [18]. The simplified structure and a sketch of the DSPMG are shown in Figure 2a, and the definitions of the *d-q* axes of the DSPMG are shown in Figure 2b. The *d*-axis is determined when the PM flux linkage of phase A is the maximum. As a result, the quadrature axis is 90° (in electrical degrees) ahead of the direct axis. The mechanical position of the *d*-axis and *q*-axis will differ by 1.41° (=90°/64) due to the 64 teeth in the rotor [11,36].
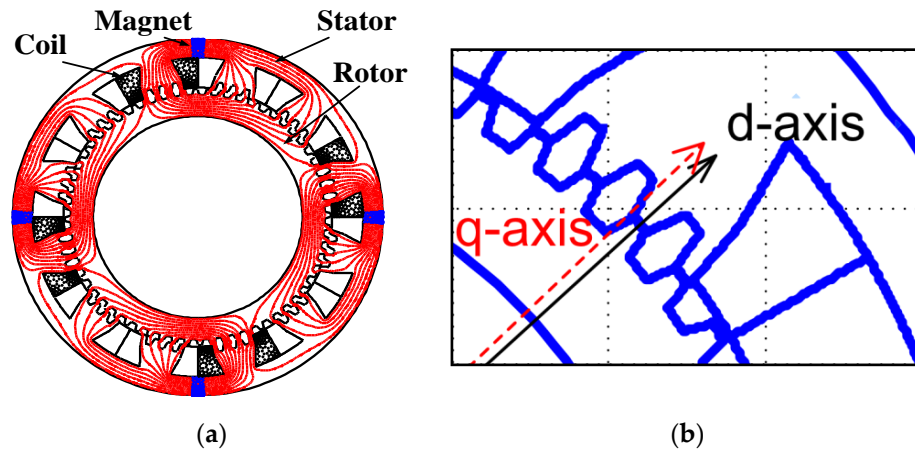
Figure 2. DSPMG structure. (**a**) Machine structure. (**b**) *d-q* axes of the machine [36].

The mathematical model of the DSPMG is different from a conventional PMSM. The model is nonlinear and the fluxes are strongly coupled. In order to simplify the analysis and the mathematical model, the second-order and higher-order Fourier terms of the self-inductance, the mutual inductance and the PM flux linkage of the DSPMG are neglected [9]. The mathematical model of the DSPMG in the *d-q* coordinate system is given as follow [9,18]:

The equations for the self-inductance and mutual inductance of the stator on the *d-q* axis are:

$$\begin{cases} L_d = L_0 - M_0 + \left(\frac{L_1}{2} + M_1\right)\cos(3\theta_e) \\ L_q = L_0 - M_0 - \left(\frac{L_1}{2} + M_1\right)\cos(3\theta_e) \\ M_{dq} = -\left(\frac{L_1}{2} + M_1\right)\sin(3\theta_e) \end{cases} \tag{2}$$

where $L_{d,q}$ are the stator inductances in the *d-q* reference frame; θ_e is the electrical angle; M_{dq} presents the mutual inductance between the *d-q* axis.

The voltage equations can be expressed as:

$$\begin{cases} u_d = -\left(R_s + 2\omega_e M_{dq}\right)i_d + \omega_e\left(\frac{3L_d}{2} - \frac{L_q}{2}\right)i_q - L_d\frac{di_d}{dt} - M_{dq}\frac{di_q}{dt} \\ u_q = -\left(R_s - 2\omega_e M_{dq}\right)i_q - \omega_e\left(\frac{3L_q}{2} - \frac{L_d}{2}\right)i_d - L_q\frac{di_q}{dt} - M_{dq}\frac{di_d}{dt} - \sqrt{\frac{3}{2}}\varphi_1\omega_e \end{cases} \tag{3}$$

where R_s is the stator resistance; i_d and i_q are the direct axis and the quadrature axis currents, respectively; ω_e is the rotor electrical angular velocity; φ_1 is the fundamental component of PM flux linkage.

The electromagnetic torque T_{em} is then given by (4):

$$T_{em} = -\left[\frac{N_r}{2}M_{dq}\left(i_d^2 - i_q^2\right) - \frac{N_r}{2}\left(L_d - L_q\right)i_d i_q + \sqrt{\frac{3}{2}}N_r\varphi_1 i_q\right] \tag{4}$$

where N_r is the teeth number of the rotor.

The machine mechanical behavior is modeled by (5):

$$J_m\frac{d\omega_m}{dt} = T_{em} + T_m - f\omega_m \tag{5}$$

where T_m is the mechanical torque; f is the viscosity coefficient; ω_m is the mechanical angular velocity; J_m is the rotor inertia.

The power equation of the DSPMG is shown in (6):

$$\begin{cases} P_{em} + P_{mec} = J_m \frac{d\omega_m}{dt}\omega_m + f\omega_m^2 \\ \omega_m = \frac{\omega_e}{N_r} \\ n = \frac{30}{\pi}\omega_m \end{cases} \tag{6}$$

where P_{em} is electromagnetic power and n is generator speed.

3. Controller Design for a DSPMG-Based TST

According to the previous section, undoubtedly, a DSPMG-based TST is a nonlinear and strongly coupled system. Moreover, it always works even with variable loads and different rotation speeds because of different tidal current speeds and complex working conditions. Thus, a suitable nonlinear and robust control algorithm is very essential for this system.

ADRC and ILC are both nonlinear control algorithms, which are independent of the controlled object mathematical model. Unfortunately, they both have their own shortcomings, which have been already discussed in the introduction. This section will develop ADRILC for the current loop to control the nonlinear system and reduce the torque ripple of the DSPMG due to the current error. As the torque ripple and the variable tidal current may also bring a fluctuation in speed, which could result in a rotor shaft problem, the hybrid control ADRC–ILC, which combines ADRC and ILC together, is deduced for the speed loop of the DSPMG-based TST.

3.1. An ADRILC-Based Current Loop Controller

For the sake of more convenient research, the current control system can be considered a nonlinear second-order system with a perturbation term [19]. The state equation is defined as Formula (7):

$$\begin{cases} \dot{x}_1(t,k) = x_2(t,k) \\ \dot{x}_2(t,k) = f(t,x) + u(t,k) \end{cases} \tag{7}$$

where x_1 and x_2 are the system state variables; $f(t,x)$ is an unknown nonlinear function; u is the signal.

First of all, in order to obtain the error of the current tracking control, a Tracking Differentiator (TD) is designed to obtain the tracking and differentiation signals of the actual and desired currents, and the TD can use smoothing processes for abrupt changes in the signal.

TD1 is designed to obtain the tracking signal $i_1(t,k)$ and differential signal $i_2(t,k)$ of the actual current signal i. The second-order discretized tracking differentiator TD1 is designed using the *fhan* function, which is given in Equation (8):

$$\begin{cases} x_{11}(t,k+1) = x_{11}(t,k) + h_1 \times x_{12}(t,k) \\ x_{12}(t,k+1) = x_{12}(t,k) + h_1 \times fhan(x_{11}(t,k)-i, x_{12}(t,k), s_1, h_1) \end{cases} \tag{8}$$

With:

$$\begin{cases} fhan(x_{11},x_{12},s_1,h_1) = \begin{cases} -s_1 sgn(a)\,, & |a| > d \\ -s_1 \frac{a}{d}\,, & |a| \leq d \end{cases} \\ d = s_1 h_1; \quad d_0 = dh_1 \\ y = x_{11} - i + h_1 x_{12} \\ a_0 = \sqrt{8s_1|y| + d^2} \\ a = \begin{cases} x_{12} + \frac{(a_0-d)}{2}sgn(y), & |y| > d_0 \\ x_{12} + \frac{y}{h_1}\,, & |y| \leq d_0 \end{cases} \end{cases} \tag{9}$$

where $x_{11} = i_1$ and $x_{12} = i_2$; y, d, d_0, a and a_0 are intermediate variables, which are used to simplify the equation; s_1 is the speed factor, which determines the tracking speed and h_1 is the filter factor. The appropriate s_1 and h_1 can effectively solve the contradiction between rapidity and overshoot, as well as the chattering problem.

TD2 is designed to obtain the tracking signal $i_1^*(t,k)$, differential signal $i_2^*(t,k)$ and second-order differential signal $i_3^*(t,k)$ of the desired current signal i^*. The third-order discretized tracking differentiator TD2 is designed in Equation (10):

$$\begin{cases} x_{21}(t,k+1) = x_{21}(t,k) + h_2 \times x_{22}(t,k) \\ x_{22}(t,k+1) = x_{22}(t,k) + h_2 \times x_{23}(t,k) \\ x_{23}(t,k+1) = x_{23}(t,k) + h_2 \times f_h \\ f_h = -c_1 s_2{}^3 x_{21}(t,k) - c_2 s_2{}^2 x_{22}(t,k) - c_3 s_2 x_{23}(t,k) + c_1 s_2{}^3 i^* \end{cases} \tag{10}$$

where $x_{21} = i_1^*$, $x_{22} = i_2^*$ and $x_{23} = i_3^*$; f_h is a nonlinear function; c_1, c_2 and c_3 are the gain coefficients; s_2 is the speed factor; h_2 is the filter factor.

The error is defined as:

$$\begin{cases} e(t,k) = x(t,k) - r(t,k) \\ e(0,k) = 0 \end{cases} \tag{11}$$

where $x = [i_1 \ i_2]^T$ and $r = [i_1^* \ i_2^*]^T$ and r is the desired signal of the state x.

According to Equations (7) and (11), the error equation can be expressed as shown in (12):

$$\begin{cases} \dot{e}_1(t,k) = e_2(t,k) \\ \dot{e}_2(t,k) = f(t,x) + u(t,k) - \dot{r}_2(t,k) \end{cases} \tag{12}$$

The system in Equation (7) is a complex nonlinear system. The system structure can be greatly simplified and the error can be reduced by reasonably designing $u(t,k)$ to compensate for the unknown item $f(t,x)$. The ESO can effectively estimate the system state or unknown items in the time domain, and cannot increase the estimation accuracy via iterative learning. Therefore, the IESO of system (8) in the iterative domain is designed to track the current reference, subsequently.

The ESO of system (7) in the time domain is given in (13) [25]:

$$\begin{cases} \dot{\hat{x}}_1(t,k) = \hat{x}_2(t,k) - \frac{a_2}{\varepsilon}(\hat{x}_1 - x_1) \\ \dot{\hat{x}}_2(t,k) = \hat{x}_3(t,k) - \frac{a_1}{\varepsilon^2}(\hat{x}_1 - x_1) + u(t,k) \\ \dot{\hat{x}}_3(t,k) = -\frac{a_0}{\varepsilon^3}(\hat{x}_1 - x_1) \end{cases} \tag{13}$$

where $\hat{x}$ is the estimated value of x and $a_{1,2,3}$ are the coefficients of the Hurwitz polynomial $s^3 + a_2 s^2 + a_1 s + a_0 = 0$ and $0 < \varepsilon \leq 1$.

Taking the following coordinate transformation:

$$\begin{cases} z_1(t,k) = \hat{x}_1(t,k) \\ z_i(t,k) = \hat{x}_i(t,k) - \sum\limits_{j=1}^{i-1} \frac{a_{n+1-j}}{\varepsilon^j}\left(z_{i-j} - x_{i-j}\right) \\ i = 2, 3, \ldots, n+1 \end{cases} \tag{14}$$

With

$$\begin{cases} z_0(t,k) = \int_0^t z_1(\tau,k)d\tau \\ x_0(t,k) = \int_0^t x_1(\tau,k)d\tau \end{cases} \tag{15}$$

According to Equations (13) and (14), Equation (13) is transformed in the following form:

$$\begin{cases} \dot{z}_1(t,k) = z_2(t,k) \\ \dot{z}_2(t,k) = -\sum\limits_{j=0}^{2} \frac{a_j}{\varepsilon^{3-j}} b_j(t,k) + u(t,k) \end{cases} \tag{16}$$

With

$$\begin{cases} b_j(t,k) = z_j(t,k) - x_j(t,k) \\ b_j(0,k) = 0 \end{cases} \tag{17}$$

From Equation (14), the following formula can be written:

$$
\begin{aligned}
|x_i(t,k) - z_i(t,k)| &= \left| x_i(t,k) - \hat{x}_i(t,k) + \sum_{j=1}^{i-1} \frac{a_{n+1-j}}{\varepsilon^j}\left(z_{i-j} - x_{i-j}\right) \right| \\
&\leq |x_i(t,k) - \hat{x}_i(t,k)| + \left| \sum_{j=1}^{i-1} \frac{a_{n+1-j}}{\varepsilon^j}\left(z_{i-j} - x_{i-j}\right) \right|
\end{aligned}
\tag{18}
$$

Therefore, $z_i(t,k)$ is the estimated value of $x_i(t,k)$ as $\hat{x}_i(t,k)$. The error equation of the transformed system (16) can be obtained as (19):

$$
\begin{cases}
\dot{b}_1(t,k) = b_2(t,k) \\
\dot{b}_2(t,k) = \hat{f}_b(t,x) + u(t,k) - \dot{x}_2(t,k)
\end{cases}
\tag{19}
$$

With

$$
\hat{f}_b(t,x) = -\sum_{j=0}^{2} \frac{a_j}{\varepsilon^{3-j}} b_j(t,k)
\tag{20}
$$

It can be found that Equations (12) and (19) have the same structural form. Equations (7) and (16) are a pair of so-called dual systems, and so are Equations (12) and (19). The IESO of system (7) in the iterative domain can be designed as (21) [26]:

$$
\begin{cases}
w_r(t,0) = 0 \\
w_r(t,k) = w_r(t,k-1) + \sum_{j=0}^{2} \frac{a_j}{\varepsilon^{3-j}} e_j(t,k)
\end{cases}
\tag{21}
$$

where $e_0(t,k) = \int_0^t e_1(\tau,k)d\tau$ and $w_r(t,k)$ is the estimated value of $f(t,x)$.

A comprehensive error is defined as follows by Equation (21) to make the coefficient of $e_2(t,k)$ equal one:

$$
\sigma(t,k) = \frac{\varepsilon}{a_2} \sum_{j=0}^{2} \frac{a_j}{\varepsilon^{3-j}} e_j(t,k)
\tag{22}
$$

From the error in Equation (12), the derivative of $\sigma(t,k)$ is shown in Equation (23):

$$
\begin{aligned}
\dot{\sigma}(t,k) &= \frac{\varepsilon}{a_2} \sum_{j=0}^{1} \frac{a_j}{\varepsilon^{3-j}} e_{j+1}(t,k) + \dot{e}_2(t,k) \\
&\frac{\varepsilon}{a_2} \sum_{j=0}^{1} \frac{a_j}{\varepsilon^{3-j}} e_{j+1}(t,k) + f(t,x) + u(t,k) - \dot{r}_2(t,k)
\end{aligned}
\tag{23}
$$

The control law is designed using Equation (24):

$$
u(t,k) = \dot{r}_2(t,k) - w_r(t,k) - \frac{\varepsilon}{a_2} \sum_{j=0}^{1} \frac{a_j}{\varepsilon^{3-j}} e_{j+1}(t,k) - \beta\sigma(t,k)
\tag{24}
$$

According to the defined error (11) and desired current signal, the current system control law is obtained:

$$
u(t,k) = i_3^* - w_r(t,k) - \frac{\varepsilon}{a_2} \sum_{j=0}^{1} \frac{a_j}{\varepsilon^{3-j}} e_{j+1}(t,k) - \beta\sigma(t,k)
\tag{25}
$$

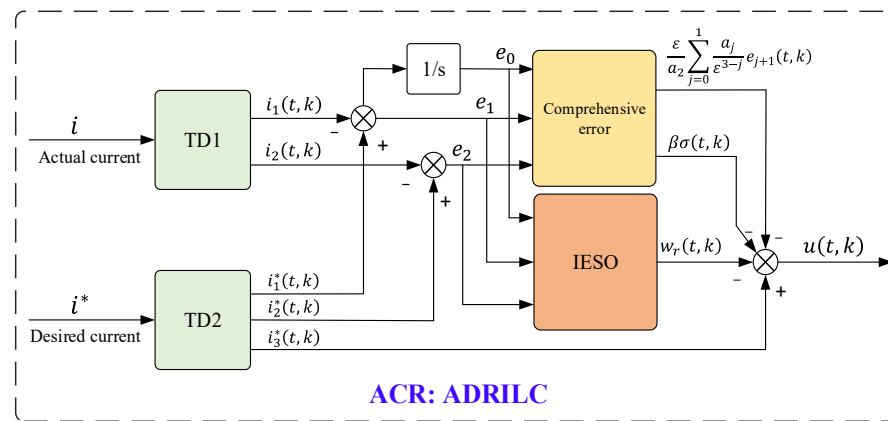According to Equation (25), the block diagram of the ADRILC-based current loop controller is shown in Figure 3.

Figure 3. A block diagram of ADRILC-based current loop controller.

3.2. ADRC–ILC-Based Speed Loop Controller

Although the mechanical system in Equation (5) can be simply considered a first-order inertial system, which could smooth the speed and reduce the speed ripple, the speed may still have some fluctuations due to the variable tidal current.

To solve the contradiction between rapidity and overshoot, and reduce the steady-state errors with variable input in traditional PI control, ADRC is used for the speed loop. This control, which has a good tracking ability, can observe the disturbance and dynamically compensate for it. Consequently, the speed can be accurately controlled even with a variable tidal current speed [37]. To further suppress the speed ripple and reduce the impact of the possible periodic torque ripple in the current loop, an ILC algorithm is also proposed. This algorithm can optimize the input error signal with an iterative method, and suppress the initial deviation of the system using the forgetting factor. The error will keep decreasing as the iteration times increase, which makes the system output as close as possible to the ideal value [38]. Therefore, the hybrid control ADRC–ILC in the speed loop can certainly improve the speed response, and suppress the speed ripple and steady-state error as well.

Based on the above analyses, a speed loop controller based on ADRC–ILC is designed subsequently. The second-order TD3 is designed as Equation (26):

$$\begin{cases} x_{31}(k+1) = x_{31}(k) + h \times x_{32}(k) \\ x_{32}(k+1) = x_{32}(k) + h \times fhan\left(x_{31}(k) - n_{ref}, x_{32}(k), s, h\right) \end{cases} \tag{26}$$

where n_{ref} is the desired value of generator speed n; x_{31} is the tracking signal of n_{ref}; x_{32} is the differential signal of n_{ref}; s is the speed factor and h is the filter factor. The appropriate s and h can effectively solve the contradiction between rapidity and overshoot.

The ESO can observe the disturbance in the speed loop and dynamically compensate for it to reduce steady-state errors in speed.

The ESO is designed:

$$\begin{cases} e = z_{n1}(k) - n \\ z_{n1}(k) = z_{n1}(k-1) + h \times [z_{n2}(k-1) - \beta_{01} \times e] \\ z_{n2}(k) = z_{n2}(k-1) + h \times [z_{n3}(k-1) - \beta_{02} \times fal(e, \alpha_1, \delta) + b_0 \times u(k)] \\ z_{n3}(k) = z_{n3}(k-1) - h \times \beta_{03} \times fal(e, \alpha_2, \delta) \end{cases} \tag{27}$$

With

$$fal(e, \alpha, \delta) = \begin{cases} \frac{e}{\delta^{1-\alpha}} & , \quad |e| \leq \delta \\ |e|^\alpha sgn(e) & , \quad |e| > \delta \end{cases} \tag{28}$$

where β_{01}, β_{02} and β_{03} are the error correction gains; α is a nonlinear factor; δ is the filter factor; e is the speed error signal; n is the actual generator speed; $z_{n1}(k)$ and $z_{n2}(k)$

are the tracking signal and the differential signal of n, respectively; $z_{n3}(k)$ is disturbance observation and b_0 is a control gain.

According to the nonlinear state error feedback control law (NLSEF), the control law of ADRC can be obtained:

$$u_1 = \beta_1 fal(e_1, \alpha_1, \delta) + \beta_2 fal(e_2, \alpha_2, \delta) - \frac{z_3}{b_0} \qquad (29)$$

where $0 < \alpha_1 < 1 < \alpha_2$; β_1 and β_2 are the gain coefficients and u_1 is the control law of ADRC, which provides the main q-axis reference current.

In order to suppress the initial deviation in the speed loop, a forgetting factor is introduced into the parallel ILC to increase the robustness of the algorithm against the noise and disturbance of the system dynamics.

The PD-type iterative learning control law with a forgetting factor is shown in Equation (30):

$$u_2 = u_{k+1}(t) = (1 - m(t))u_k(t) + m(t)u_0(t) + G_P e_k(t) + G_D \dot{e}_k(t) \qquad (30)$$

where $m(t)$ is the forgetting factor; $u_0(t) = 0$ is the initial input of ILC; $u_k(t)$ is the kth input of ILC; G_P and G_D are all the learning gains; $e_k(t)$ is the speed error and u_2 is the control signal, namely, the reference compensation q-axis current generated using ILC.

Based on the above analysis, the control law of an ADRC–ILC-based speed loop controller is designed, which is given in (31):

$$u = u_1 + u_2 \qquad (31)$$

According to Equations (26), (27) and (31), a block diagram of the speed loop control based on ADRC–ILC is shown in Figure 4.
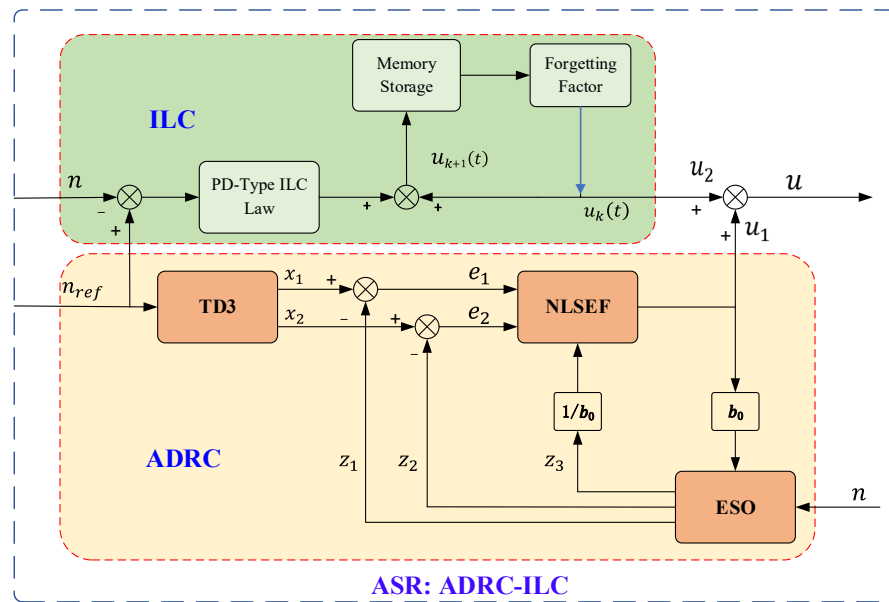

Figure 4. A block diagram of ADRC–ILC-based speed loop controller.

4. Control Strategy for the System

Considering the variable tidal current speed, the strategies for the tidal current energy conversion system at both low and high tidal current speeds will be proposed and analyzed in this section, for when the tidal current speed is at or below the rated speed (rated tidal current speed $V_{tide} = 2.5$ m/s). In a previous study [18], the OTSR-based MPPT strategy is adopted to find the optimum rotor speed and extract the maximum tidal current energy. When the tidal current speed is above the rated speed, the LAFWC is proposed to ensure the

system works stably and limit the generator power to the rated value. Figure 5 represents the control scheme of the system, and a flowchart of the system is shown in Figure 6.
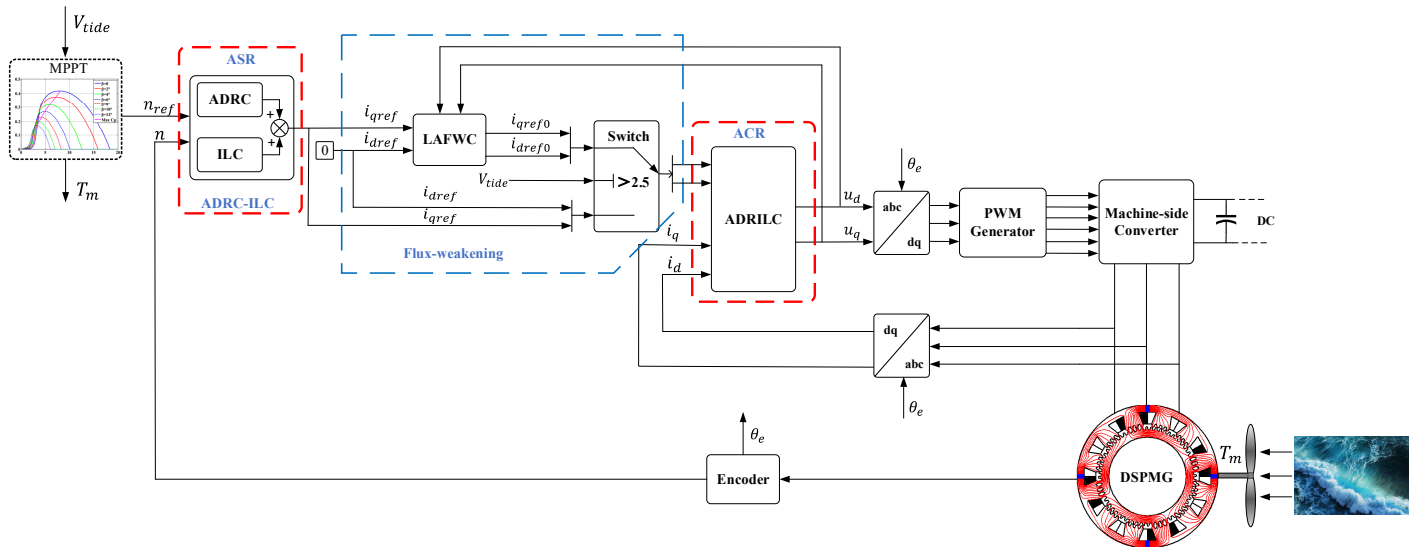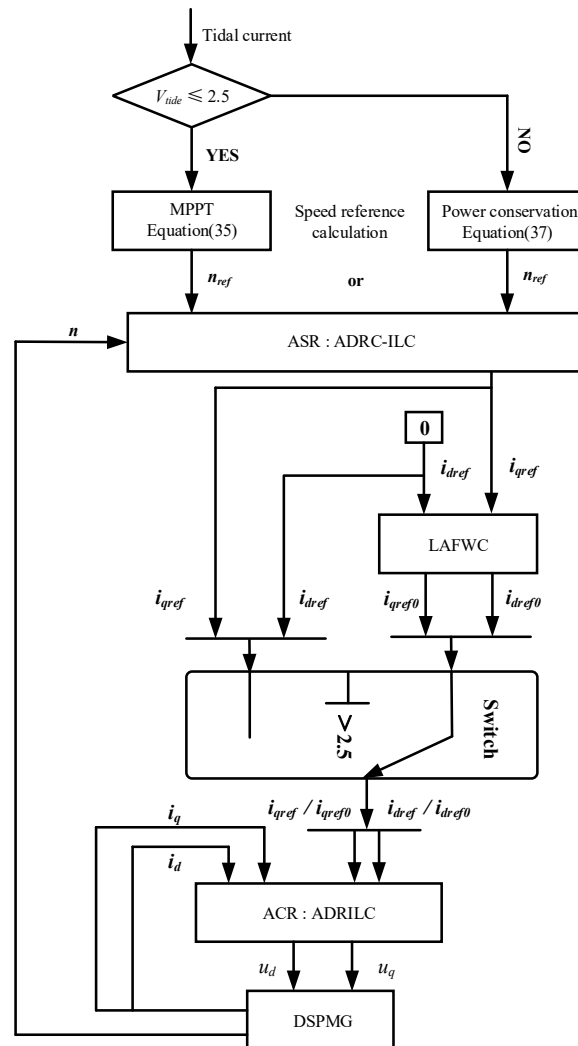

Figure 5. Control scheme of system.

Figure 6. A flowchart of system.

4.1. Leading Angle Flux-Weakening Control

The idea of LAFWC is to control the leading angle to increase the demagnetization current of the *d*-axis to create a weak field. As shown in Figure 7, the angle γ, which is the angle between the stator current vector i_s and the *q*-axis, is the leading angle. When the tidal current speed is at or below the rated speed, the leading angle γ is zero, which means $i_{dref} = 0$ control method. And γ should be raised to increase the demagnetization current of the *d*-axis under high speed.
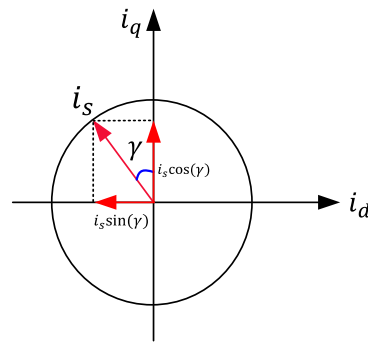

Figure 7. The leading angle.

The current and voltage limitation equations are expressed as follows:

$$i_d^2 + i_q^2 \leq I_{\max}^2 \tag{32}$$

$$u_d^2 + u_q^2 \leq u_{\max}^2 \tag{33}$$

where $u_{\max}$ and $I_{\max}$ are the maximum allowable phase voltage and current, and $u_{\max} = \frac{1}{\sqrt{3}} u_{dc}$, under space vector PWM, u_{dc} is the voltage of the DC bus; $I_{\max}$ is determined by the machine and converter power ratings.

Then, the equation for the corrected currents can be expressed as follows:

$$\begin{cases} i_{dref0} = i_s \sin(\gamma) \\ i_{qref0} = i_s \cos(\gamma) \end{cases} \tag{34}$$

where i_{dref0} and i_{qref0} are the corrected value of i_{dref} and i_{qref} under flux-weakening control; $i_{dref} = 0$ and i_{qref} is the output of the ASR.

As the voltage harmonics could influence the current, the Butterworth filter is adopted to reduce higher harmonics in the voltage and reduce the corrected current ripple. Meanwhile, the integral windup of the PI controller may lead the leading angle γ to become too large. The demagnetization current i_{dref0} will exceed the limitation and increase the current and torque ripple. An anti-windup method is proposed to limit the value of γ. When γ is over the limit, the integral coefficient will be removed and only the proportionality coefficient be reserved to make the controller exit the saturation state. A block diagram of the proposed LAFWC is shown in Figure 8.
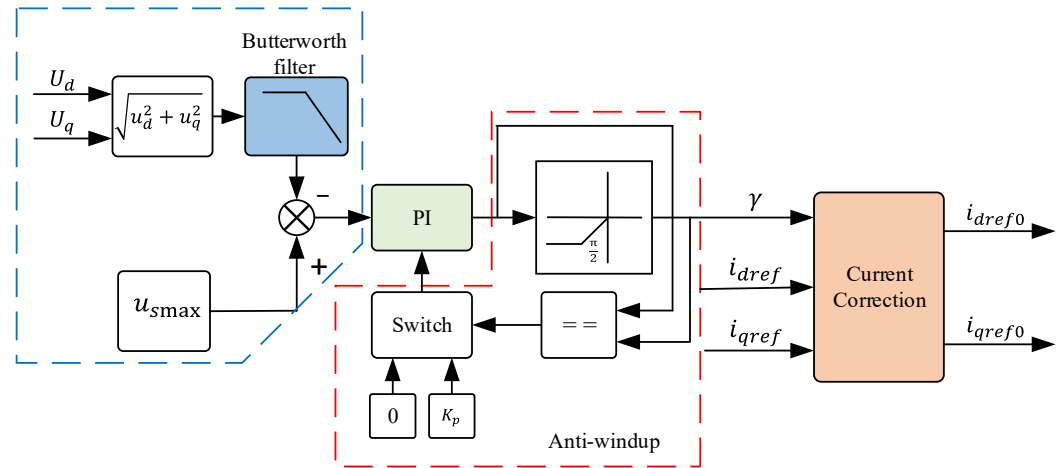
Figure 8. A block diagram of LAFWC.

4.2. Determination of a Mechanical Angular Velocity Reference in the Flux-Weakening Region

When the tidal current speed is at or below the rated speed, the mechanical speed ω_{mref} can be calculated under a OTSR-based MPPT strategy to obtain the OTSR λ_{opt} and the maximum power coefficient C_p.

$$\omega_{mref} = \frac{\lambda_{opt} V_{tide}}{R} \tag{35}$$

where R is the radius of the TST.

When the tidal current speed is over the rated value, the MPPT mode should be changed to flux-weakening mode. In this case, the mechanical angular velocity reference ω_{mref} should be determined by the turbine power conservation. The mechanical power P_m is expressed as Equation (36):

$$P_m = P_e + f\omega_{mref}^2 \tag{36}$$

where P_e is the desired electromagnetic power.

According to Equation (1), the power conservation equation can be rewritten as follows:

$$
\begin{aligned}
P_e + f\omega_{mref}^2 &= \tfrac{1}{2}C_p\rho A V_{tide}^3 \\
&= \tfrac{1}{2}C_p\rho \times \pi R^2 \times \frac{\omega_{mref}^3 R^3}{\lambda^3} \\
&= \frac{C_p}{\lambda^3} \times \frac{\pi\rho R^5}{2} \times \omega_{mref}^3
\end{aligned} \tag{37}
$$

Undoubtedly, the C_p curve will work on the right part ($\lambda > \lambda_{opt}$) under an excessive speed. As shown in Figure 9, the coefficient $\frac{C_p}{\lambda^3}$ is monotonically decreasing in the right part of the C_p curve. Consequently, the curve of P_{mec} is a set of curves, which is as shown in Figure 10 from the C_1 curve to the C_2 curve. According to Equation (37) there is always a definite solution with a different coefficient $\frac{C_p}{\lambda^3}$. All the determined solutions correspond one to one to the intersection points of the curve of P_m and curves P_{mec}, which is the BC curve. As shown in Figure 10, ω_{mMPPT} is the rated mechanical angular velocity reference corresponding to the rated tidal current speed. For the BC curve, once the tidal current speed above the limit is determined, the corresponding desired mechanical angular velocity reference ω_{mref} can be obtained.
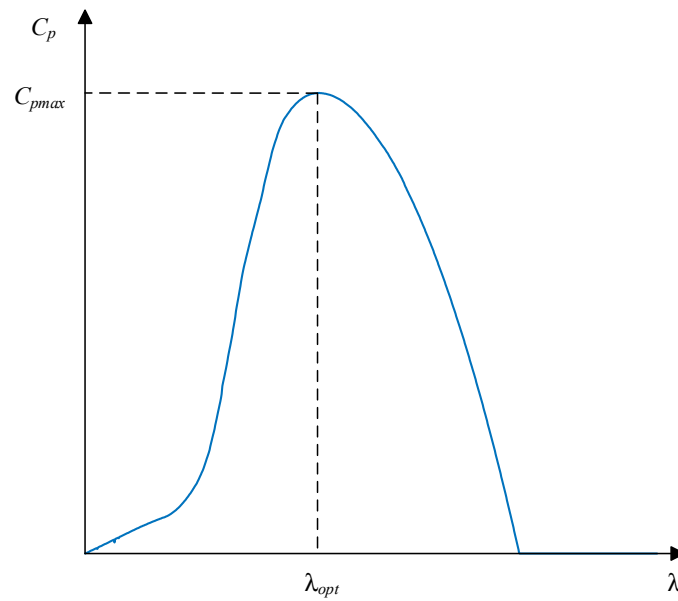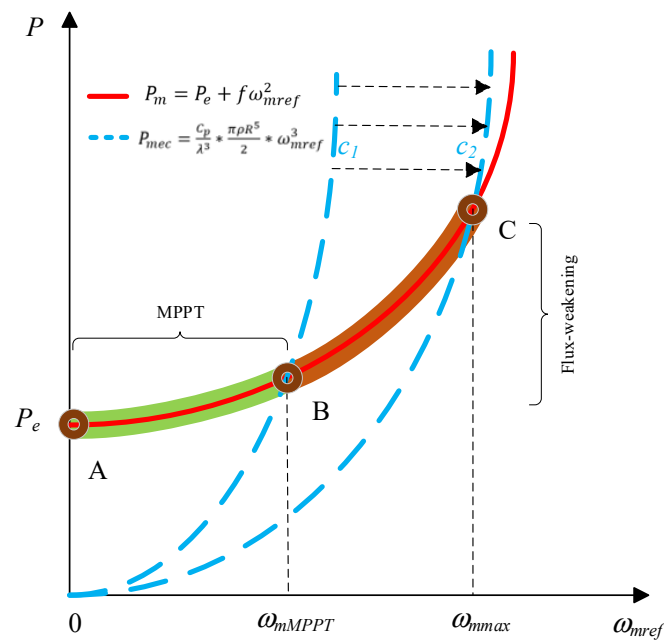
Figure 9. The C_p curve of the TST.

Figure 10. The power curves.

5. Simulation and Analysis

Based on the control algorithms and strategies presented in the in Sections 3 and 4, simulation results are shown in this section. Firstly, a simplified tidal current speed, which is at or below the rated speed, is used to validate the steady-state and dynamic performance of ADRC–ILC + ADRILC. To better verify the relative effectiveness and superiority, several different control algorithms based on classic PI, ILC and ADRC in Table 1 are compared. Then, the performance analysis of the proposed control is discussed. Finally, the tidal current speed considering the swell effect is established to verify the effectiveness of the control strategy. The machine parameters used in this paper are given in Table 2.

Table 1. Control algorithms.

Control Algorithms ASR + ACR	Speed Loop Control Algorithms	Current Loop Control Algorithms
PI + PI	PI	PI
PI + ILC	PI	ILC
PI + ADRILC	PI	ADRILC
ADRC + ADRILC	ADRC	ADRILC
ADRC–ILC + ADRILC	ADRC–ILC	ADRILC

Table 2. Parameters of DSPMG [19].

Parameters	Symbol	Value
Self-inductance	L_0/L_1	25.5/2.5 mH
Mutual-inductance	M_0/M_1	−12.4/2.5 mH
Stator resistance	R_s	88.37 mΩ
Rotor tooth number	N_r	64

5.1. Comparative Study of Different Controls

In reality, the tidal current speed cannot be always regarded as constant for a long time, mainly because of the complicated underwater environment and the influence of the sea state. Therefore, the control performance of a DSPMG-based TST can be evaluated using a variable different tidal current speed at different stages. In this part, in order to thoroughly compare the performances of different control algorithms, the tidal current speed is limited to the rated value. The simplified tidal current speed is 2 m/s at the beginning, suddenly jumps to 2.5 m/s at 1 s and then remains until the end.

In reality, the mechanical response time of the TST should be in seconds. Due to the limitations of software, the response time in the simulation is set to around 100 ms for simplification. Nevertheless, this setting can still reflect the dynamic response of the system for comparison.

Based on this, the parameters of the different control algorithms proposed above are rigorously determined. Figure 11a,b clearly show the speed response and torque of different control algorithms, respectively. The detailed simulation results are presented in Tables 3 and 4.
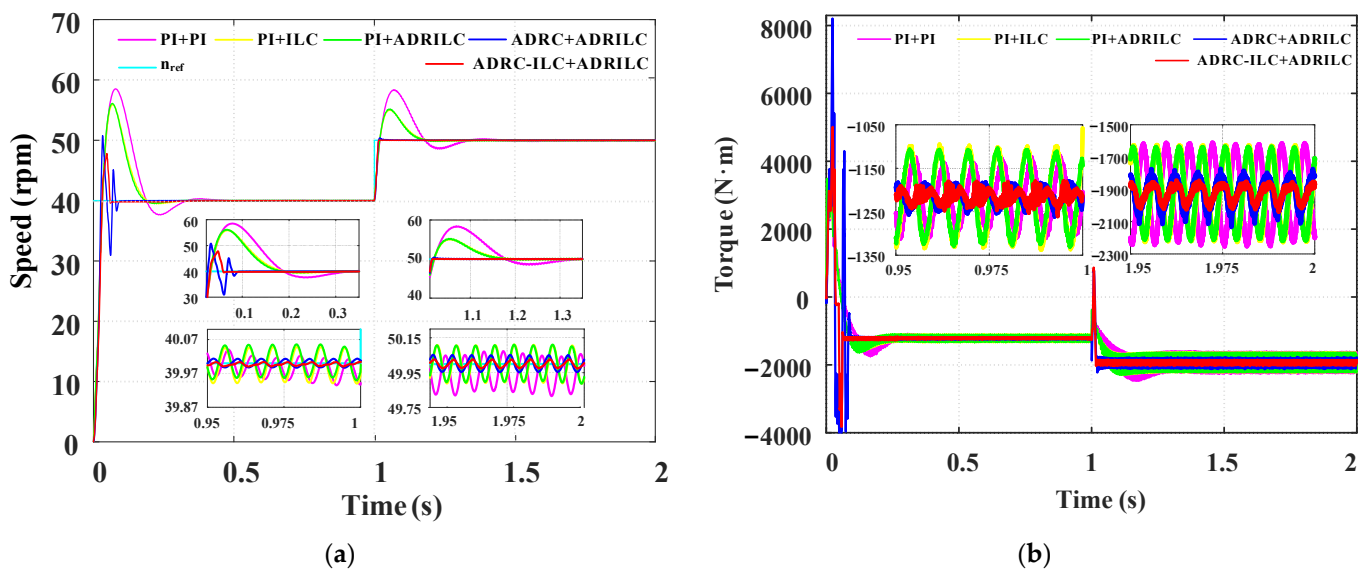

Figure 11. Simulation results of different control algorithms. (**a**) Generator speed *n*. (**b**) Electromagnetic torque T_{em}.

Table 3. Comparison of the speed response for different algorithms.

Tidal Speed (m/s)	2.0		2.5	
Indicators	D_1	Steady-State Error (rpm)	D_2	Steady-State Error (rpm)
PI + PI	43.30%	0.106	83.7%	0.260
PI + ILC	39.76%	0.108	50.85%	0.223
PI + ADRILC	40.24%	0.099	51.8%	0.217
ADRC + ADRILC	26.83%	0.026	4.2%	0.099
ADRC–ILC + ADRILC	19.47%	0.015	0.3%	0.052

Table 4. Comparison of torque ripple coefficient η for different algorithms.

Tidal Speed (m/s)	2.0			2.5		
Indicators	T_{em} (Nm)	T_{ave} (Nm)	η	T_{em} (Nm)	T_{ave} (Nm)	η
PI + PI	$[-1316, -1115]$	-1215.5	16.54%	$[-2256, -1608]$	-1932	33.54%
PI + ILC	$[-1338, -1095]$	-1216.5	19.98%	$[-2225, -1627]$	-1926	31.05%
PI + ADRILC	$[-1331, -1101]$	-1216	18.91%	$[-2222, -1635]$	-1928.5	30.44%
ADRC + ADRILC	$[-1269, -1169]$	-1219	8.20%	$[-2132, -1774]$	-1953	18.33%
ADRC–ILC + ADRILC	$[-1255, -1176]$	-1215.5	6.50%	$[-2037, -1846]$	-1941.5	9.84%

To describe the effect of different control algorithms in reducing the torque ripple and speed overshoot more clearly and intuitively, the torque ripple coefficient η and speed overshoot D are defined using the following equations:

$$\eta = \left| \frac{T_{max} - T_{min}}{T_{ave}} \right| \times 100\% \tag{38}$$

where T_{max} and T_{min} are the maximum and minimum values of the electromagnetic torque, respectively, and T_{ave} is the average value of the electromagnetic torque at a steady state.

$$\begin{cases} D_1 = \frac{n_{2max} - n_{2ref}}{n_{2ref}} \\ D_2 = \frac{n_{2.5max} - n_{2.5ref}}{n_{2.5ref} - n_{2ref}} \end{cases} \tag{39}$$

where D_1 and D_2 are the speed overshoot when the tidal speed is 2.0 m/s and 2.5 m/s, respectively. n_{2max} and n_{2ref} are the maximum speed and reference speed of the generator at 2.0 m/s. $n_{2.5max}$ and $n_{2.5ref}$ are the maximum speed and reference speed of the generator at 2.5 m/s.

From Figure 11a, the different algorithms could all follow the speed reference at different tidal current speeds. This reflects that a DSPMG-based TST can operate reliably. However, the speed has an overshoot inevitably at the start-up stage due to the fast external mechanical response. Indeed, the overshoot could be reduced by changing the control parameters, and the transient process should be smoother. Their overall variation trend will not change.

Table 3 presents the details of the speed response for different algorithms. In Table 3, when the speed loop adopts the classic PI control, the speed overshoot is more than 40% with 2.0 m/s and more than 50% with 2.5 m/s regardless of the current loop with PI, ILC or ADRILC. Moreover, the steady-state errors of the system speed are around 0.1 rpm and 0.2 rpm, respectively, for these two tidal current speeds.

If ADRILC is selected as the ACR, with the different controllers (PI, ADRC, ADRC–ILC) used in the speed loop, the overshoot is highly reduced from 40.24% to 19.47% at 2.0 m/s and from 51.8% to 0.3% at 2.5 m/s. In addition, for these two tidal current speeds, the steady-state errors are also continuous reduced from about 0.1 rpm to 0.015 rpm and from 0.217 rpm to

0.052 rpm, respectively. From this figure and table, we can see that ADRC and ADRC–ILC can overcome the contradiction between the rapidity and overshoot of the speed response. Because of the adoption of ILC, ADRC–ILC could still improve the attenuation oscillation and reduce the repetitive disturbances.

From Figure 11b, it can be obviously observed that ADRC–ILC + ADRILC has the minimum torque ripple for at 2 m/s and 2.5 m/s. From Table 4, the first three control algorithms with the same ASR (PI) involve relatively large torque ripple coefficients, more than 15% for 2 m/s and more than 30% for 2.5 m/s. Although PI + PI can obtain the smallest η (16.54%) for 2 m/s, it is at the cost of the speed overshoot and regulating time. In addition, when the current speed reaches 2.5 m/s, the torque ripple coefficient η of this algorithm becomes the biggest, up to 33.54%. ADRILC can achieve a relatively smaller η than ILC even with the same ASR (PI) at these two tidal current speeds. It can be proved that PI + ADRILC is slightly better than PI + ILC in this system.

For the last three algorithms, which use the different ASR but the same ACR, obviously, the system performance should be better. With different ASRs (PI, ADRC, ADRC–ILC), the torque ripple will be highly decreased from 18.91% to 6.50% at 2.0 m/s and from 30.44% to 9.84% at 2.5 m/s. All these results reflect that the choice of ASR is also quite essential for this system, especially for the input of the ACR. Combined with the results in Table 3, the smaller the steady-state error in speed, the smaller the torque ripple.

Another point to mention is that the torque ripple coefficient η increases with speed for every algorithm. There are two possible reasons for this phenomenon. Firstly, with an increased speed, the current frequency should be raised, as the iterative learning algorithm cannot obtain a suitable compensation current in a shorter period. Secondly, due to the system nonlinearity and the variable input, ADRILC may not follow the reference well, especially for higher harmonic current components. The current error would be increased with the increasing speed and the resulting current error causes the torque ripple.

Based on analyses above, ADRC–ILC + ADRILC is the best combination in terms of the speed response and torque ripple reduction for a DSPMG-based TST in this section. The superiority of ADRC–ILC + ADRILC is fully proved compared with the other algorithms.

5.2. Analysis of the Proposed Control for MPPT and LAFWC Strategies

5.2.1. Current Analysis

To further verify the effectiveness of the ADRC–ILC + ADRILC, the three-phase currents of the system are presented and analyzed. Fast Fourier Transformation (FFT) is applied to the phase current for this purpose. In this part, the actual currents will be compared with the theoretically calculated values, as well as their spectral characteristics. The theoretically calculated currents are expressed in Appendix A, and have been determined from [9]. The three-phase currents are given in Figures 12–15 to show the current comparisons at 2.0 m/s, 2.5 m/s and 2.6 m/s tidal current speeds, respectively.

It can be seen from Figure 12 that the frequency of the three-phase currents increases with a raised tidal current speed. The amplitude of the currents increases with a raised tidal current speed for the MPPT strategy, and decreases for the LAFWC strategy. Although the waveform of the phase current is asymmetrical, the sum of the three-phase currents is equal to 0. It means that this current must contain some even harmonic components, which corresponds to the theoretical analysis developed in [9]. Some more comparisons are presented in Figures 13–15.

In Figures 13–15, the currents of the DSPMG at three different tidal current speeds are presented. In general, from Figures 13a, 14a and 15a, the currents under the proposed control algorithm at these three speeds are very similar to the theoretical currents. Apparently, the errors between the actual currents and theoretical currents are within around 1.5 A, 2.0 A and 5 A, respectively. From these three figures, the three current errors have similar waveforms. To be more precise, they may mainly contain certain even harmonic components, as they have four local minimums and four local maximums in one period. Figures 13b, 14b and 15b just reveal the first five important current harmonic components.

Apparently, this control algorithm could track the fundamental very well. The error of the fundamental should be smaller than 0.5 A even at 2.5 m/s and 2.6 m/s tidal speeds. This is the main factor that generates the torque. The amplitudes of the fifth and seventh harmonic currents are relatively small and the relative errors are also very slight. However, the second and fourth components all have relatively bigger errors. The errors are about 0.5 A at a 2.0 m/s tidal speed and reach up to around 1 A at 2.5 m/s and 2.6 m/s. This could fully explain the waveforms of the current errors. According to the previous research in [9], these two harmonics are used for torque ripple compensation. These differences would surely deteriorate the compensation effect.
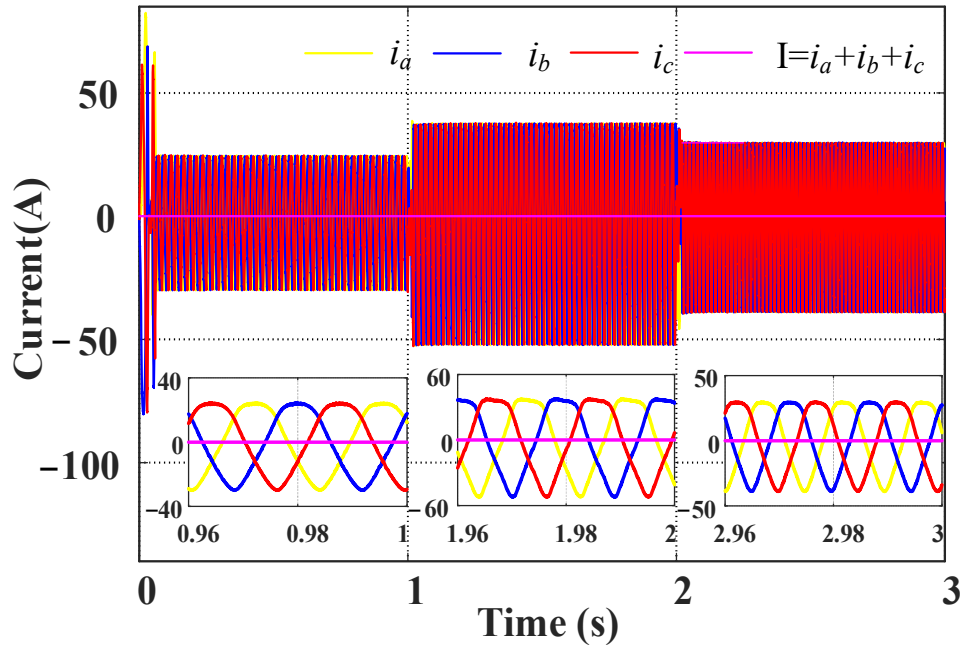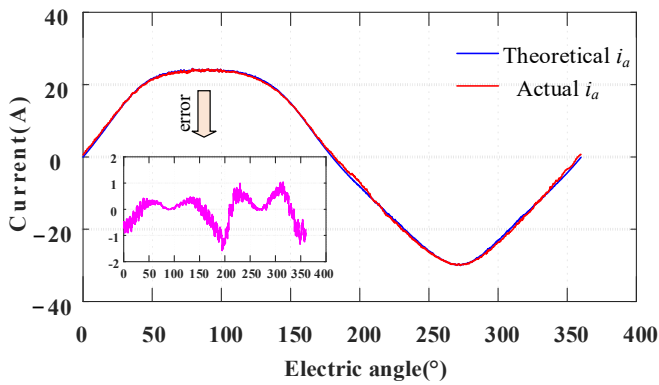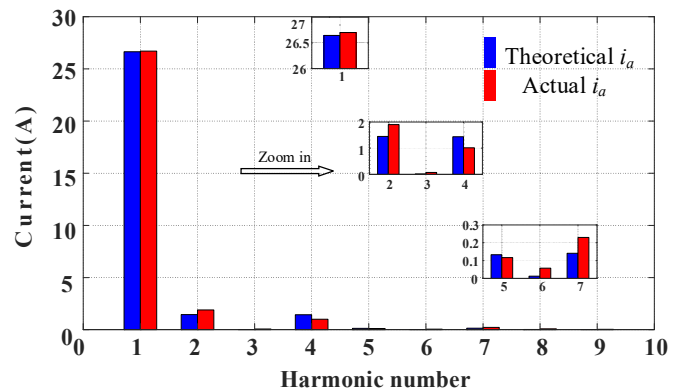

Figure 12. The three-phase currents.

(**a**)   (**b**)

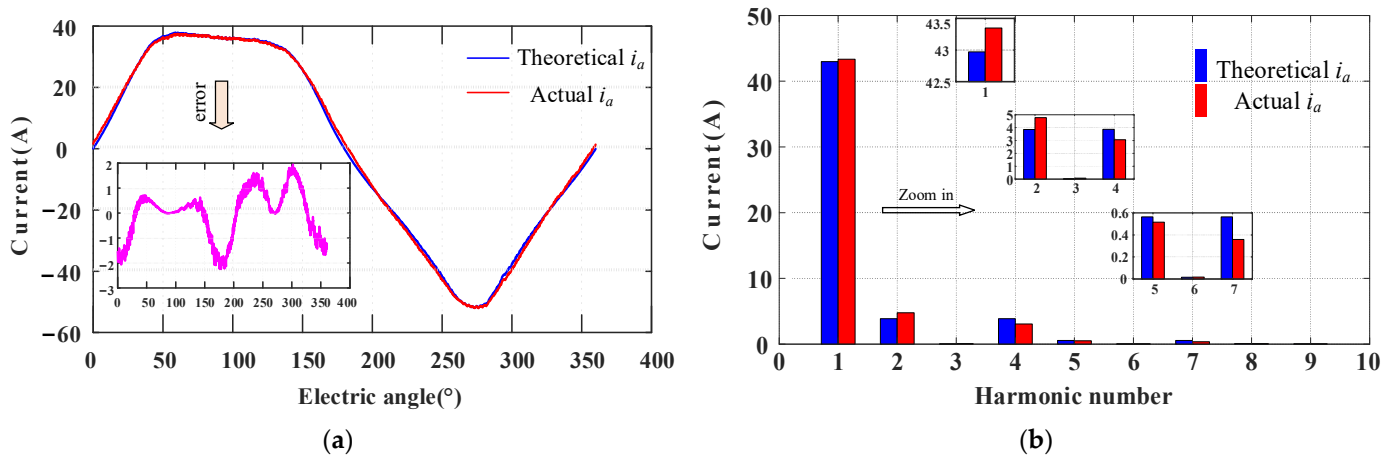**Figure 13.** Current comparison when tidal current speed is 2.0 m/s. (**a**) Phase current i_a. (**b**) FFT of the current.

Figure 14. Current comparison when tidal current speed is 2.5 m/s. (**a**) Phase current i_a. (**b**) FFT of the current.
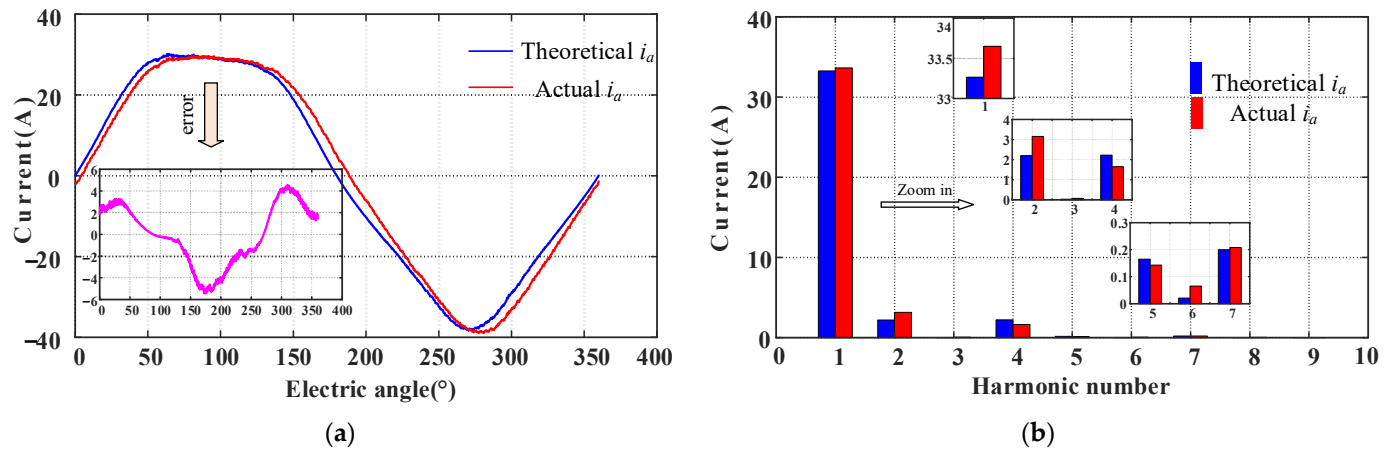

Figure 15. Current comparison when tidal current speed is 2.6 m/s. (**a**) Phase current i_a. (**b**) FFT of the current.

5.2.2. Robustness Analysis

Based on the analyses above, ADRC–ILC + ADRILC has the best performance, obviously. As the complicated environment may perturb the DSPMG parameters, the robustness of this control algorithm will be analyzed for the MPPT and LAFWC strategies in this section with respect to variation in the self-inductance L_1 and stator resistance R_s.

In Figure 16a,b, the values of L_1 and R_s in the DSPMG model vary between 0.8 and 1.2 of their initial values. The comparative details of the performance with different conditions are presented in Tables 5 and 6.

From Figure 16a, when L_1 or R_s changes, the system almost keeps the same speed response. From Table 5, compared with the initial steady-state error of the speed, when R_s or L_1 changes, the speed errors are almost the same, 0.01 rpm for 2.0 m/s, 0.05 rpm for 2.5 m/s and 0.02 rpm for 2.6 m/s. The only difference is that the variation in L_1 will change the speed error. When L_1 is smaller, the speed error becomes smaller, and vice versa.

Figure 16b and Table 6 present the performance of the torque based on variables L_1 or R_s in detail. The same phenomenon appears again. With variation in R_s at different tidal current speeds, the torque ripple coefficients are almost the same. To be more specific, the change in R_s has an opposite but negligible effect on η and the speed error. While for L_1, when L_1 changes, η will also change with the same variation tendency. The change in this value is still very small and acceptable.
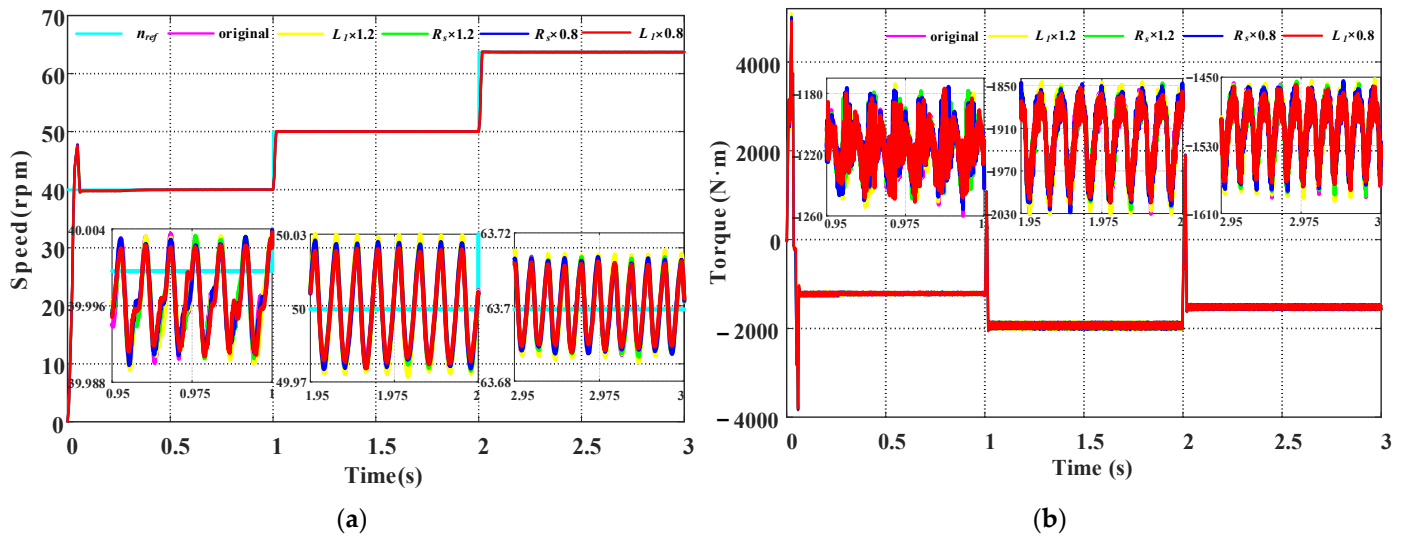
(**a**)   (**b**)

Figure 16. Robustness analysis under the influence of L_1 or R_s. (**a**) Generator speed. (**b**) Electromagnetic torque.

Table 5. Comparison of speed response with variable L_1 or R_s.

Tidal Speed (m/s)	2.0	2.5	2.6
Condition	Steady-State Error (rpm)		
Original	0.015	0.052	0.025
$R_s \times 0.8$	0.014	0.053	0.025
$R_s \times 1.2$	0.014	0.052	0.024
$L_1 \times 0.8$	0.013	0.047	0.022
$L_1 \times 1.2$	0.015	0.058	0.029

Table 6. Comparison of torque ripple coefficient η with variable L_1 or R_s.

Tidal speed (m/s)	Condition	T_{em} (Nm)	T_{ave} (Nm)	η
2.0	Original	[−1255, −1176]	−1215.5	6.50%
	$R_s \times 0.8$	[−1254, −1172]	−1213	6.76%
	$R_s \times 1.2$	[−1256, −1178]	−1217	6.41%
	$L_1 \times 0.8$	[−1251, −1175]	−1213	6.27%
	$L_1 \times 1.2$	[−1256, −1174]	−1215	6.75%

Table 6. *Cont.*

	2.5			2.6		
	T_{em} (Nm)	T_{ave} (Nm)	η	T_{em} (Nm)	T_{ave} (Nm)	η
	[−2038, −1846]	−1942	9.89%	[−1590, −1456]	−1523	8.80%
	[−2029, −1851]	−1940	9.18%	[−1578, −1464]	−1521	7.50%
	[−2034, −1846]	−1940	9.69%	[−1588, −1464]	−1526	8.13%
	[−2033, −1842]	−1937.5	9.86%	[−1581, −1455]	−1518	8.30%
	[−2037, −1846]	−1941.5	9.84%	[−1588, −1462]	−1525	8.26%

From the details in Table 6, two issues should also be explained: (1) The inductance L_1 has a greater influence on torque ripple than R_s; (2) The changes in L_1 and R_s lead to different variation tendencies.

In terms of the first issue, this is mainly because, on the one hand, the inductance L_1 is directly linked to the torque by Equation (4). On the other hand, the resistance R_s is not directly linked with the torque. If the current changes, the system may need a different iteration time to compensate for the torque ripple. In terms of the second issue, this is mainly due to the variation in the electromagnetic time constant determined by L_1 and R_s. Based on the basic definition, the electromagnetic time constant has the same variation tendency as L_1 but the opposite tendency as R_s. If the electromagnetic time constant is smaller, the current can track the reference more quickly, and vice versa. The resulting current error would generate greater torque ripple.

According to the above analyses, we can conclude that ADRC–ILC + ADRIL is a robust control algorithm.

5.3. System Performance Validation

In order to testify the performance of the whole system with the MPPT and flux-weakening strategies, the tidal current speed based on the practical model is established to verify the effectiveness of the strategy. The tidal current speed considering the swell effect is shown in Figure 17. The relative generator speed is presented in Figure 18, which displays a good speed tracking performance.

The mechanical power P_m, electromagnetic power P_{em} and generator power P are given in Figure 19. It can be observed that the electromagnetic power P_{em} is fixed to about 10 kW for a tidal current speed over 2.5 m/s, and the generated power is slightly less than the electromagnetic power due to the copper loss. Figure 20 shows the electromagnetic torque with a variable tidal current speed. Obviously, the electromagnetic torque will decrease when the tidal current is higher than 2.5 m/s. These simulation results all verify that the flux-weakening strategy proposed for an excessive tidal current speed is effective in conserving the electromagnetic power and increasing the generator speed.
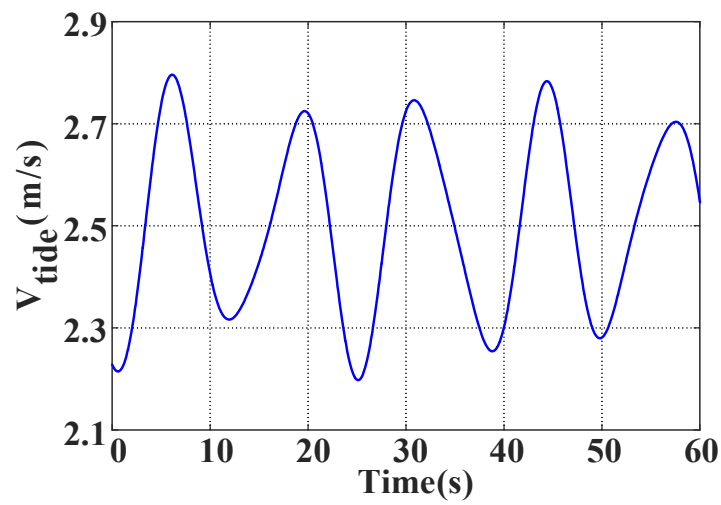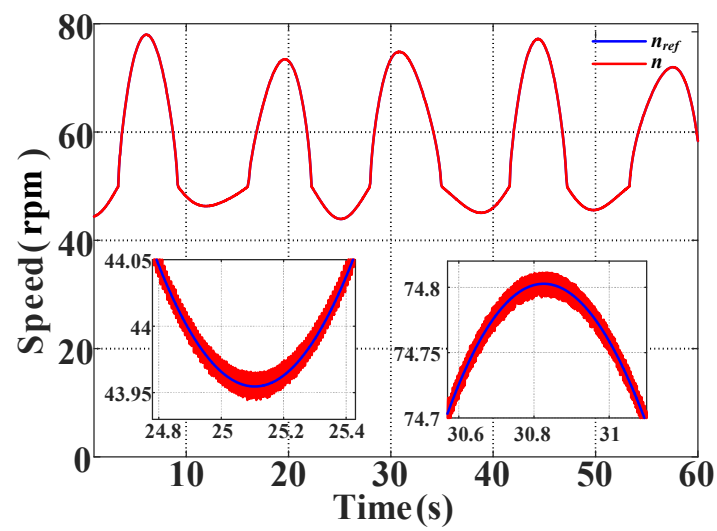
Figure 17. Tidal current speed.
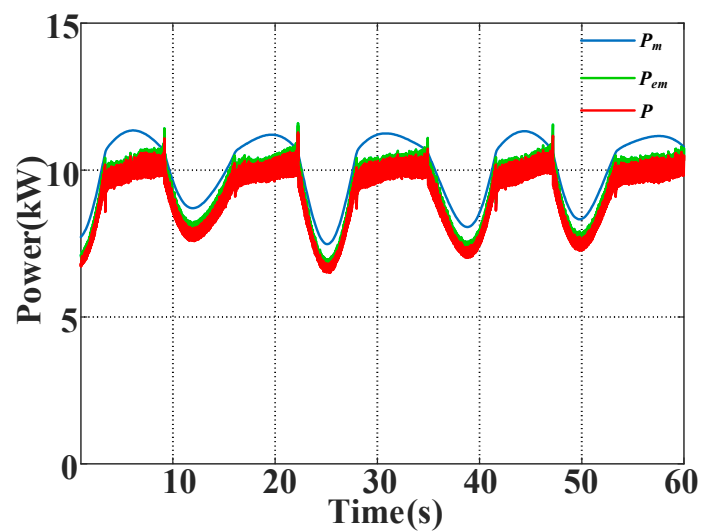
Figure 18. Generator speed.
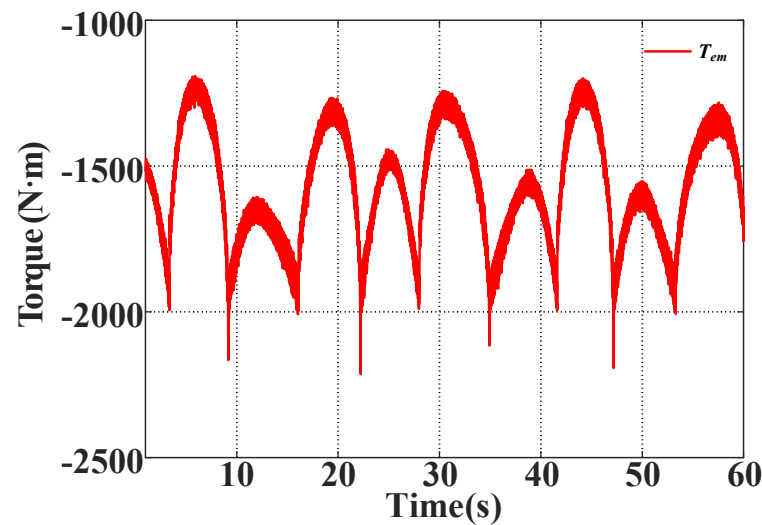
Figure 19. Power performances.

Figure 20. Electromagnetic torque.

6. Conclusions

This paper deals with the control algorithms and strategies for a DSPMG-based TST. OTSR-based MPPT (for a low tidal current speed) and LAFWC strategies (for a high tidal current speed) are proposed for the system. Based on the system model and the characteristic analysis, several model-free control algorithms are proposed to reduce the torque ripple and the speed steady-state error and improve the system robustness. The proposed ADRC–ILC + ADRILC algorithm is independent of the mathematical model of the controlled object. ADRC–ILC uses ADRC to deal with the external non-periodic speed ripple and adopts ILC to reduce the internal periodic speed ripple, simultaneously. ADRILC employs an iterative method to improve the ESO for the enhancement of the convergence rate of ILC. Accordingly, the system response speed can be improved and the torque ripple can be decreased more thoroughly.

The simulation results fully verify the superiority and effectiveness of ADRC–ILC + ADRILC, which appears to be the most attractive option in this study. The proposed control strategy has a good torque performance in the simplified DSPMG model. In addition, it can almost obtain the theoretical current, and has very excellent robustness. This has already made a big step forward in the BLAC mode of a DSPMG. System performance validation presents the effectiveness of the LAFWC. It is well designed to extend the operating range and conserve the electromagnetic power at a high tidal current speed. This work provides a meaningful control method for the development and application of a DSPMG-based TST in the future.

Author Contributions: Conceptualization, H.C. and L.L.; methodology, H.C. and L.L.; software, H.C. and L.L.; validation, H.C. and L.L.; writing—original draft preparation, H.C. and L.L.; writing—review and editing, H.C., L.L., Y.A., Z.Z., N.A.-A. and M.B.; visualization, L.L.; supervision, H.C., Y.A., Z.Z., N.A.-A. and M.B.; project administration, H.C.; funding acquisition, H.C. All authors have read and agreed to the published version of the manuscript.

Institutional Review Board Statement: Not applicable.

Informed Consent Statement: Not applicable.

Data Availability Statement: The data that support the findings of this study are available within the article.

Nomenclature

ACR	Automatic Current Regulator
ADRC	Active Disturbance Rejection Control
ADRC–ILC	Active Disturbance Rejection Control–Iterative Learning Control
ADRILC	Active Disturbance Rejection-Based Iterative Learning Control
ASR	Automatic Speed Regulator
DSPMG	Doubly Salient Permanent Magnet Generator
DSPMM	Doubly Salient Permanent Magnet Machine
ESO	Extended State Observer
ILC	Iterative Learning Control
LAFWC	Leading Angle Flux-Weakening Control
MFC	Model-Free Control
MPPT	Maximum Power Point Tracking
OTSR	Optimal Tip Speed Ratio
PM	Permanent Magnet
TST	Tidal Stream Turbine
V_{tide}	tidal current speed (m/s)
P_{TST}	mechanical power of tidal stream turbine (W)
P_m	mechanical power of machine (W)
P_{hyd}	hydrodynamic power (W)
C_p	power coefficient
A	swept area of the turbine (m^2)
ρ	ocean density (kg/m^3)
ω_m	mechanical angular velocity (rad/s)
n	generator speed (rpm)
P_{em}	electromagnetic power (W)
u_d, u_q	direct axis and the quadrature axis voltages (V)
i_d, i_q	direct axis and the quadrature axis currents (A)
L_d, L_q	direct axis and the quadrature axis inductances (H)
M_{dq}	mutual inductance between direct axis and the quadrature axis (H)
ω_e	electrical angular velocity (rad/s)
θ_e	electrical angle (rad)
φ_1	PM flux linkage fundamental
L_0, L_1	fundamental and first harmonic inductances (H)
M_0, M_1	fundamental and first harmonic mutual inductance (H)
J_m	rotor inertia (kg $\times$ m^2)
f	viscosity coefficient (Nm·s/rad)
N_r	the teeth number of the rotor
η	torque ripple coefficient

Appendix A

The quasi-sinusoidal current in a three-phase stationary coordinate system is shown in Equation (A1):

$$\begin{cases} i_a = -I_m(\theta_e)\sin(\theta_e + \theta_0) \\ i_b = -I_m(\theta_e)\sin\left(\theta_e - \frac{2\pi}{3} + \theta_0\right) \\ i_c = -I_m(\theta_e)\sin\left(\theta_e + \frac{2\pi}{3} + \theta_0\right) \end{cases} \tag{A1}$$

where $I_m(\theta_e)$ is the quasi-sinusoidal current amplitude, which varies with electrical angle θ_e, and θ_0 is the equivalent load angle.

Meanwhile, the formula for the basic electromagnetic torque can be rewritten as follows:

$$T_{em} = -\left[\frac{3}{2}\mathrm{N}_r\varphi_1\cos\theta_0 I_m(\theta_e) + \frac{3}{4}\mathrm{N}_r\left(\frac{L_1}{2} + M_1\right)\sin(3\theta_e + 2\theta_0)I_m^2(\theta_e)\right] \tag{A2}$$

Because the current has to be an actual value in theory, the amplitude of this current is shown in Equation (A3).

$$I_m(\theta_e) = \frac{-\frac{3}{2}\mathrm{N}_r\varphi_1\cos\theta_0 + \sqrt{\left(\frac{3}{2}\mathrm{N}_r\varphi_1\cos\theta_0\right)^2 - 3\mathrm{N}_r\left(\frac{L_1}{2} + M_1\right)\sin(3\theta_e + 2\theta_0)T_{em}}}{\frac{3}{2}\mathrm{N}_r\left(\frac{L_1}{2} + M_1\right)\sin(3\theta_e + 2\theta_0)} \tag{A3}$$

References

1. Touimi, K.; Benbouzid, M.; Tavner, P. Tidal stream turbines: With or without a Gearbox? *Ocean Eng.* **2018**, *170*, 74–88. [CrossRef]
2. Leijon, M.; Nilsson, K. Direct electric energy conversion system for energy conversion from marine currents. *Proc. Inst. Mech. Eng. Part A J. Power Energy* **2007**, *221*, 201–205. [CrossRef]
3. Guerroudj, C.; Saou, R.; Boulayoune, A.; Zaïm, M.E.-H.; Moreau, L. Performance analysis of Vernier slotted doubly salient permanent magnet generator for wind power. *Int. J. Hydrogen Energy* **2017**, *42*, 8744–8755. [CrossRef]
4. Cheng, M.; Zhang, G.; Hua, W. Overview of Stator Permanent Magnet Brushless Machine Systems and Their Key Technologies. *Proc. Chin. Soc. Electr. Eng.* **2014**, *34*, 5204–5220.
5. Rezzoug, A.; Zaïm, M.E.H. *Non-Conventional Electrical Machines*; John Wiley and Sons: Hoboken, NJ, USA, 2011.
6. Guerroudj, C.; Saou, R.; Charpentier, J.F.; Boulayoune, A. Optimal Design of a Novel Doubly Salient Permanent Magnet Motors for High Power Ship Propulsion. In Proceedings of the 2018 XIII International Conference on Electrical Machines, Alexandropolis, Greece, 3–6 September 2018; pp. 2556–2562.
7. Guerroudj, C.; Charpentier, J.-F.; Saou, R.; Karnavas, Y.L.; Bracikowski, N.; Zaïm, M.E.-H. Coil Number Impact on Performance of 4-Phase Low Speed Toothed Doubly Salient Permanent Magnet Motors. *Machines* **2021**, *9*, 137. [CrossRef]
8. Sun, J.; Wang, A.; Wang, T.; Jin, Y. Torque Ripple of Doubly Salient PM Motor Affected by Stator and Rotor Tooth Pole Structure. *Electr. Mach. Technol.* **2019**, *3*, 32–36.
9. Chen, H.; Tang, T.; Han, J.; Aït-Ahmed, N.; Machmoum, M.; Zaïm, M.E.-H. Current waveforms analysis of toothed pole Doubly Salient Permanent Magnet (DSPM) machine for marine tidal current applications. *Int. J. Electr. Power Energy Syst.* **2019**, *106*, 242–253. [CrossRef]
10. Cheng, M.; Hua, W.; Zhu, X.Y.; Zhao, W.X.; Jia, H.Y. A simple method to improve the sinusoidal static characteristics of doubly-salient PM machine for brushless AC operation. In Proceedings of the 2007 International Conference on Electrical Machines and Systems, Seoul, Republic of Korea, 8–11 October 2007; pp. 665–669.
11. Hua, W.; Cheng, M. A new model of vector-controlled doubly-salient permanent magnet motor with skewed rotor. In Proceedings of the 2008 International Conference on Electrical Machines and Systems, Wuhan, China, 17–20 October 2008; pp. 3026–3031.
12. Pan, X.Q.; Zhu, X.Y.; Zuo, Y.F.; Zhang, C.; Quan, L. The Current Suppression of Doubly Salient Permanent Magnet Motor with Non-Rare-Earth. *Mot. Control. Appl.* **2017**, *44*, 72–78.
13. Liu, J.F.; Zhu, X.Y.; Quan, L.; Xiang, Z.X.; Zhang, C. Driving Control Research of Less-rare-earth Tooth Yoke Magnetomotive Complementary Doubly Salient Permanent Magnet Motors Based on Resonance Compensation Strategy. *Proc. Chin. Soc. Electr. Eng.* **2017**, *37*, 6534–6542.
14. Xu, W.; Yang, W.; Yu, X.; He, J. One new model based predictive torque control algorithm for doubly salient permanent magnet synchronous machines. In Proceedings of the IECON 2012 38 the Annual Conference on IEEE Industrial Electronics Society, Montreal, QC, Canada, 25–28 October 2013; pp. 4133–4138.
15. Xu, W.; Qu, R.; Yang, W. New model based predictive current control strategy for doubly salient permanent magnet synchronous machines. In Proceedings of the 2013 IEEE Energy Conversion Congress and Exposition (IEEE-ECCE), Denver, CO, USA, 15–19 September 2013; pp. 1450–1457.
16. Yang, Y.; Wang, Q.; Hu, Y.; Wu, Q.; Xiao, L.; Zhang, Z. Multiple Sine-Wave Superposition Drive for the Doubly Salient Motor Based on Fourier Linearization Modeling. *IEEE Trans. Power Electron.* **2021**, *37*, 4419–4430. [CrossRef]
17. Cheng, H.; Cui, J.; Peng, C.; Chu, J.; Zhou, J.; Ye, Z. Electromagnetic Characteristics Analysis and Torque Ripple Reduction for Doubly Salient PM Machine. *IEEE Trans. Energy Convers.* **2023**, *38*, 1659–1668. [CrossRef]
18. Chen, H.; Ait-Ahmed, N.; Machmoum, M.; Zaim, M.E.-H. Modeling and Vector Control of Marine Current Energy Conversion System Based on Doubly Salient Permanent Magnet Generator. *IEEE Trans. Sustain. Energy* **2016**, *7*, 409–418. [CrossRef]
19. Chen, H.; Li, Q.; Tang, S.; Aït-Ahmed, N.; Han, J.; Wang, T.; Zhou, Z.; Tang, T.; Benbouzid, M. Adaptive super-twisting control of doubly salient permanent magnet generator for tidal stream turbine. *Int. J. Electr. Power Energy Syst.* **2021**, *128*, 106772. [CrossRef]
20. Pan, Z.P.; Luo, X.B. Torque Ripple Minimization of Switched Reluctance Motor Based on Iterative Learning Control. *Trans. China Electrotech. Soc.* **2010**, *25*, 51–55.

21. Qian, W.; Panda, S.; Xu, J. Speed Ripple Minimization in PM Synchronous Motor Using Iterative Learning Control. *IEEE Trans. Energy Convers.* **2005**, *20*, 53–61. [CrossRef]
22. Mohammed, S.A.Q.; Nguyen, A.T.; Choi, H.H.; Jung, J.-W. Improved Iterative Learning Control Strategy for Surface-Mounted Permanent Magnet Synchronous Motor Drives. *IEEE Trans. Ind. Electron.* **2020**, *67*, 10134–10144. [CrossRef]
23. Han, J. From PID to Active Disturbance Rejection Control. *IEEE Trans. Ind. Electron.* **2009**, *56*, 900–906. [CrossRef]
24. Wang, B.; Tian, M.; Yu, Y.; Dong, Q.; Xu, D. Enhanced ADRC With Quasi-Resonant Control for PMSM Speed Regulation Considering Aperiodic and Periodic Disturbances. *IEEE Trans. Transp. Electrif.* **2021**, *8*, 3568–3577. [CrossRef]
25. Li, X.Y.; Tian, S.; Ai, W. Active disturbance rejection based iterative learning control. In Proceedings of the 2016 Chinese Control and Decision Conference, Yinchuan, China, 28–30 May 2016; pp. 6645–6650.
26. Li, X.Y. Iterative extended state observer and its application in iterative learning control. *Control. Decis.* **2015**, *30*, 473–478.
27. Morimoto, S.; Sanada, M.; Takeda, Y. Effects and Compensation of Magnetic Saturation in Flux-Weakening Controlled Permanent Magnet Synchronous Motor Drives. *IEEE Trans. Ind. Appl.* **1994**, *30*, 1632. [CrossRef]
28. Yoon, Y.-D.; Sul, S.-K. New flux weakening control for surface mounted permanent magnet synchronous machine using gradient descent method. In Proceedings of the 2007 7th International Conference on Power Electronics, Daegu, Republic of Korea, 22–26 October 2007; pp. 1208–1212.
29. Zhang, Z.; Wang, C.; Zhou, M.; You, X. Flux-Weakening in PMSM Drives: Analysis of Voltage Angle Control and the Single Current Controller Design. *IEEE J. Emerg. Sel. Top. Power Electron.* **2018**, *7*, 437–445. [CrossRef]
30. Park, J.; Jung, S.; Ha, J.-I. Variable Time Step Control for Six-Step Operation in Surface-Mounted Permanent Magnet Machine Drives. *IEEE Trans. Power Electron.* **2017**, *33*, 1501–1513. [CrossRef]
31. Bai, S. Flux-weakening control of permanent magnet synchronous motor using leading angle. In Proceedings of the 2011 International Conference on Electrical Machines and Systems, Beijing, China, 20–23 August 2011; pp. 1–5.
32. Li, Y.; Lipo, T.A. A doubly salient permanent magnet motor capable of field weakening. In Proceedings of the PESC'95—Power Electronics Specialist Conference, Atlanta, GA, USA, 18–22 June 1995; Volume 1, pp. 565–571.
33. Chau, K.T.; Jiang, J.Z.; Wang, Y. A novel stator doubly fed doubly salient permanent magnet brushless machine. *IEEE Trans. Magn.* **2003**, *39*, 3001–3003. [CrossRef]
34. Couch, S.J.; Bryden, I. Tidal current energy extraction: Hydrodynamic resource characteristics. *Proc. Inst. Mech. Eng. Part M-J. Eng. Marit. Environ.* **2006**, *220*, 185–194. [CrossRef]
35. Bahaj, A.; Myers, L. Fundamentals applicable to the utilisation of marine current turbines for energy production. *Renew. Energy* **2003**, *28*, 2205–2211. [CrossRef]
36. Chen, H.; Ait-Ahmed, N.; Machmoum, M.; Zaim, M.E.; Schaeffer, E. Modeling and current control of a double salient permanent magnet generator (DSPMG). In Proceedings of the 2013 15th European Conference on Power Electronics and Applications (EPE), Lille, France, 2–6 September 2013; pp. 1–10.
37. Li, S.P.; Xie, Y.; Zhang, K.; He, Y.T. PMSM Direct Torque Control Based on Nonlinear Active Disturbance Rejection Controller. *Comput. Appl. Softw.* **2021**, *38*, 41–45.
38. Dai, B.L.; Gong, J. Iterative Learning Control with Forgetting Factor Based on Initial State Learning. *Inf. Control* **2018**, *47*, 547–552.